


**Controlling interlayer magnetic coupling in the two-dimensional magnet  $\text{Fe}_3\text{GeTe}_2$** In Kee Park,<sup>1</sup> Cheng Gong,<sup>2,\*</sup> Kyoo Kim,<sup>3,†</sup> and Geunsik Lee<sup>1,‡</sup><sup>1</sup>*Department of Chemistry, Center for Superfunctional Materials, Center for Wave Energy Materials, Ulsan National Institute of Science and Technology (UNIST), Ulsan 44919, Republic of Korea*<sup>2</sup>*Department of Electrical and Computer Engineering, Quantum Technology Center (QTC), University of Maryland, College Park, Maryland 20742, USA*<sup>3</sup>*Korea Atomic Energy Research Institute, Daejeon 34057, Republic of Korea* (Received 1 June 2021; revised 1 October 2021; accepted 14 December 2021; published 5 January 2022)

Interlayer magnetic coupling in emerging two-dimensional layered magnets holds great potential for manipulating layered magnetic structures for cross-layer transport or tunneling phenomena. In this paper, we employed first-principles calculations to show enhanced ferromagnetic (FM) interlayer exchange coupling for  $\text{Fe}_3\text{GeTe}_2$  by reducing stacking symmetry or reducing the layer number. Electronic structure analysis reveals that the former is mainly due to low-symmetry enhanced interlayer orbital hopping, and the latter originates from reduced Pauli potential for out-of-plane metallic electrons with respect to thicker layers. Interlayer FM coupling could also be weakened by substrates due to the screened Coulomb interactions, simulated by reducing the onsite Coulomb repulsion for Fe  $d$  electrons. In this paper, we provide guidance to rationally control interlayer magnetic coupling via engineering stacking configuration and dielectric environment.

DOI: [10.1103/PhysRevB.105.014406](https://doi.org/10.1103/PhysRevB.105.014406)**I. INTRODUCTION**

Magnetically ordered van der Waals (vdW) layered materials [1–3] hold great promise as building blocks in spintronic devices for next-generation information technology. Their inherently weak interlayer coupling allows easy access to ferromagnetic (FM) and antiferromagnetic (AFM) interlayer magnetic states even without inserting spacing materials (e.g., magnetic tunnel junctions and hetero-interfaces), and hence, their distinct cross-layer electrical resistances have been reported [4,5]. A critical parameter to study multiple interlayer magnetic states is interlayer exchange coupling, which is strongly related to the total energy difference between FM and AFM states. A variety of magnetic states beyond the collinear FM and AFM can exist owing to the perturbative coupling between spin and orbitals, which is beneficial for neuromorphic computing [6], or one could tune interlayer exchange coupling to realize topological magnons based on inverted acoustic and optical magnons [7]. However, the microscopic interlayer exchange coupling mechanism and the approaches to control it have rarely been understood and developed, particularly for  $\text{Fe}_3\text{GeTe}_2$  (FGT). The evolution from hard FM in thin FGT into soft FM in thicker FGT [8] indicates the coexisting FM and AFM interlayer configurations [9]. It remains an open question whether such behavior originates from stacking symmetry, such as  $\text{CrI}_3$  whose tunable interlayer exchange coupling has been extensively studied [10–20], or from the intrinsic layered-dependent electronic

structure. Band renormalization [21] analysis indicates that FGT is close to a strongly correlated system with probable quantum phase transformation under slight variations in onsite Coulomb repulsion strength or kinetic hopping parameters.

In this paper, we investigate the microscopic interlayer exchange coupling mechanism and its control for FGT using first-principles calculations. Stacking configuration and layer thickness effects were investigated by varying the onsite Coulomb parameter. Two crystal features were found to enhance FM interlayer exchange coupling almost independently via low-symmetry stacking enhanced interlayer orbital hopping and surface-induced Pauli potential reduction. Onsite Coulombic interaction also has significant effects, with favorable interlayer exchange coupling type switchable to AFM by a slight reduction of the Coulomb interaction. Thus, nonlocal substrate screening could be an effective approach to tailor the interlayer FM coupling in FGT. The calculated sufficiently small stacking-fault energy suggests that experimental realization of stacking engineering is feasible via both chemical synthesis and artificial mechanical construction. In this paper, we provide valuable guidance to rationally control the interlayer exchange coupling in FGT.

**II. COMPUTATIONAL METHODS**

All density functional theory (DFT) calculations were performed using the Vienna *Ab initio* Simulation Package (VASP) [22,23]. Different exchange-correlation functional types were examined with and without including the Hubbard Coulomb interaction for Fe  $d$  electrons in the Liechtenstein scheme [24], where the major behavior for different  $J$  values can be described singly in terms of  $U-J$  (Fig. S1 in the Supplemental Material [25]); thus, our results obtained for

\*gongc@umd.edu

†kyoo@kaeri.re.kr

‡gslee@unist.ac.kr

$J = 0$  are applicable to other  $J$  values with an associated value of  $U - J$  and will be presented against  $U_{\text{eff}} = U - J$  in this paper, and vdW functionals, such as TS and vdW-optB86b, were also considered. We used a plane-wave energy cutoff of 400 eV, with k-meshes  $18 \times 18 \times 2$  and  $18 \times 18 \times 1$  for bulk and bilayer, respectively. The k-meshes used for HSE06 calculations are  $6 \times 6 \times 2$  and  $12 \times 12 \times 1$ , respectively, while the vacuum layer of  $15 \text{ \AA}$  was considered to model the slab bilayer system. Structural optimization was performed using the force criteria  $0.02 \text{ eV/\AA}$ . All calculations were performed without including spin-orbit coupling, but the main conclusion would be the same when spin-orbit coupling is included. Exchange coupling constants were calculated using the Green's function method [26]. The magnetic Hamiltonian is  $H_{\text{spin}} = -\sum_{i,j} J_{ij} \hat{\mathbf{e}}_i \cdot \hat{\mathbf{e}}_j$ , where  $J_{ij} = (1/2\pi) \int_{-\infty}^{\epsilon_F} d\epsilon \text{Im Tr}[\Delta_i G_{ij}^{\uparrow} \Delta_j G_{ji}^{\downarrow}]$  is a magnetic exchange parameter between Fe spins at sites  $i$  and  $j$ ;  $\Delta_i = \int d\mathbf{k} [H_{ii}^{\uparrow}(\mathbf{k}) - H_{ii}^{\downarrow}(\mathbf{k})]$ ,  $G_{ij}^{\uparrow/\downarrow}(\epsilon) = \int d\mathbf{k} [\epsilon + E_F - H^{\uparrow/\downarrow}(\mathbf{k})]_{ij}^{-1}$  are  $5 \times 5$  matrices spanned by five Fe  $d$  orbitals; and  $H^{\uparrow/\downarrow}(\mathbf{k})$  are DFT Hamiltonians projected into Wannier basis functions [27]. This allows atomic orbital analysis by tracing over a specific type in Fe  $d$  orbitals after proper transformation onto crystal field axes. The screened onsite Coulomb interaction parameter by constrained random phase approximation  $P^{\text{cRPA}} = P_d + P_r$  was calculated with five  $d$  orbitals for one Fe for  $P_d$  and the rest maximally localized Wannier orbitals (Fe- $s$ ,  $p$ ,  $d$ , Ge- $p$ , Te- $p$ , Mo- $d$ ) for  $P_r$ . We employed a k-mesh  $6 \times 6 \times 1$ , which was sufficient for effective  $U$  convergence. The in-plane lattice parameter of the FGT/MoTe<sub>2</sub> heterosystem was fixed as the experimental value, extending the Mo-Te bond length and maintaining the bond angle (Te-Mo-Te) to preserve the main features for a pristine MoTe<sub>2</sub> electronic structure.

### III. RESULTS AND DISCUSSION

Figure 1(a) shows three possible FGT stacking types with two-layer periodicity along the out-of-plane direction. The monolayer comprises five atomic layers with the central layer forming a Fe<sup>II</sup>Ge honeycomb lattice, then the next two layers form vertical Fe<sup>I</sup> dumbbells, and the outermost two layers have Te atoms above and below Fe<sup>II</sup>. When FGT layers are vdW stacked, energetically stable and favorable structures should have every Te atom at either of two adjacent Te layers at the vdW contact adsorb at the hollow site of the other Te layer. The hollow sites form two types with stacking sequence  $ab-ca$  or  $ab-ab$  for Fe<sup>I</sup>Te-TeFe<sup>I</sup> where “-” denotes the vdW gap, and  $a$ ,  $b$ , and  $c$  denote three different in-plane coordinates  $(0,0)$ ,  $(\frac{1}{3}, \frac{2}{3})$ ,  $(\frac{2}{3}, \frac{1}{3})$ , respectively, and Fig. 1(a) shows their crystal structures (indicated by  $H_0$  and  $H_1$ ). Here,  $H_0$  and  $H_1$  belong to the same space group  $P6_3/mmc$  (No. 194), where the experimental structure [28] corresponds to  $H_0$ . Upper and lower layers in the unit cell for  $H_0$  and  $H_1$  are related by  $180^\circ$  rotation about the horizontal  $C_2$  axis in the vdW gap [Fig. 1(a), crosses]. Otherwise, two layers in the unit cell are simply related by lateral translations, and two hollow stacking types produce one equivalent crystal structure with sequence  $ab-cb$  [Fig. 1(a),  $H_2$ ] and space group  $P\bar{6}m_2$  (No. 187) without the inversion center present for  $H_0$  and  $H_1$ .

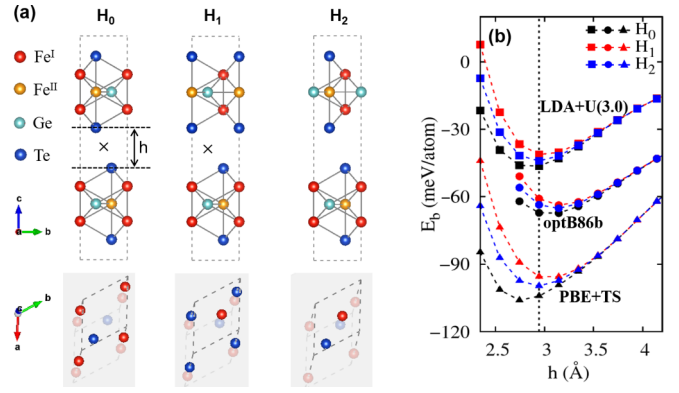


FIG. 1. Stacking types and interlayer binding energies for Fe<sub>3</sub>GeTe<sub>2</sub> (FGT). (a) Side view for FGT unit cell for three possible van der Waals (vdW) stacking types and associated top views of four interfacial atomic layers Fe<sup>I</sup>Te-TeFe<sup>I</sup> with lower and upper two atomic layers shaded and unshaded, respectively, to show different in-plane coordinates. Crosses in the vdW gap for  $H_0$  and  $H_1$  indicate the horizontal  $C_2$  rotation axis. (b) Interlayer binding energies with respect to vertical distance  $h$  [as shown in (a)] for three stacking types, where the different symbols indicate different density functional theory (DFT) functionals (LDA +  $U$  = square, optB86b = circle, and PBE + TS = triangle) employed to calculate  $E_b = E_{\text{bulk}} - 2E_{\text{ML}}$ , where  $E_{\text{bulk}}$  and  $E_{\text{ML}}$  are total energies for bulk per unit cell and monolayer, respectively, and dashed lines are only for guidance.

Figure 1(b) shows interlayer binding energies calculated for bulk FGT of FM interlayer exchange coupling with respect to interlayer distance ( $h$ ) but maintaining experimental intralayer atomic positions. We examined different exchange-correlation functional forms within DFT with Hubbard  $U_{\text{eff}}$  and vdW dispersion corrections. Figure S2 in the Supplemental Material [25] compares calculated experimental equilibrium distances with experimental  $h^{\text{exp}} = 2.95 \text{ \AA}$  for  $H_0$ . Local density approximation (LDA) or Perdew-Burke-Ernzerhof (PBE) predicted shorter or longer equilibrium distance  $h^{\text{LDA}} = 2.85 \text{ \AA}$  or  $h^{\text{PBE}} = 3.45 \text{ \AA}$ , respectively. Including Hubbard  $U_{\text{eff}} = 3 \text{ eV}$  has little influence on equilibrium distance for LDA +  $U$  or PBE +  $U$ . Adding dispersion correction to PBE reduced  $h^{\text{PBE}}$  to  $2.75 \text{ \AA}$  within PBE + TS, and optB86b-vdW produced the most plausible result  $3.05 \text{ \AA}$  among the examined functionals. These results are consistent with previous studies [29,30], with fully optimized lattice parameters by optB86b-vdW  $a = 3.99 \text{ \AA}$ ,  $c = 16.37 \text{ \AA}$  showing good agreement with experimental  $a^{\text{exp}} = 3.99 \text{ \AA}$ ,  $c^{\text{exp}} = 16.33 \text{ \AA}$ .

Figure 1(b) shows the results by three representative functionals. Binding energy strongly depends on functional type, varying as much as  $\sim 50 \text{ meV/atom}$ , indicating significant effect from electron correlation, where electron mass enhancement [31] and Kondo lattice behavior [32] have been previously observed experimentally. Calculations are consistent with previous theoretical reports, in that using LDA +  $U$ , PBE, and optB86b-vdW overestimate Fe spin magnetic moments as  $m(\text{Fe}^{\text{I}}) \approx 2.8 \mu_B$  and  $m(\text{Fe}^{\text{II}}) \approx 2.0 \mu_B$ , whereas experimental  $m(\text{Fe})^{\text{exp}} \approx 1.6 \mu_B$  [31]. Properly describing electron correlation using PBE with dynamical mean-field

theory (DMFT) shows that  $m(\text{Fe}^I) = 1.60 \mu_B$  and  $m(\text{Fe}^{II}) = 1.54 \mu_B$  with mild band renormalization by 0.6 to match well with experimental spectra [21].

Thus, no DFT method has successfully provided the full description for FGT structural, magnetic, and spectral properties [29,33–35], except sophisticated methods such as DFT + DMFT without structural relaxation. Nevertheless, Fig. 1(b) shows consistent relative stability about stacking type remains for different functionals, with  $H_0$  being most stable,  $H_1$  least stable, and  $H_2$  intermediate. Full structural optimizations using optB86b-vdW give the binding energies =  $-66.3$ ,  $-62.8$ , and  $-64.1$  meV/atom for  $H_0$ ,  $H_1$ , and  $H_2$ , respectively, with only  $\sim 2$  meV/atom difference between  $H_0$  and  $H_2$ . This is of the same order as the vdW stacking fault energy ( $10 \text{ mJ/m}^2 \sim 1 \text{ meV}/\text{\AA}^2$ ) for graphene or hBN [36], indicating probable stacking-type disorder or interfacial inversion symmetry breaking by  $H_2$  leading to nonvanishing antisymmetric interlayer exchange coupling in multilayer FGT. Significant stacking faults have been reported previously for structurally similar materials such as  $\alpha$ -RuCl<sub>3</sub> [37], Fe<sub>4</sub>GeTe<sub>2</sub> [38], and Fe<sub>5- $\delta$</sub> GeTe<sub>2</sub> [39,40]. Fe<sub>5</sub>GeTe<sub>2</sub> strongly depends on synthesis conditions, e.g., for quenching; hence, stacking fault severity can be significantly altered [40]. Hence, there could be an optimal synthesis condition for some metastable FGT structure. External pressure can also be applied to tune stacking type, as shown elsewhere for bilayer CrI<sub>3</sub> [17].

We used LDA +  $U$ , varying  $U_{\text{eff}} = 0-4$  eV to investigate stable interlayer spin configurations. Total energy difference between AFM and FM configurations  $\Delta E = E_{\text{AFM}} - E_{\text{FM}}$  was calculated, where we used experimental intralayer atomic positions and interlayer distance ( $h^{\text{exp}}$ ) to exclude other structural effects.

Figure 2(a) shows that the calculated  $H_0$  realizes stable AFM configuration for  $U_{\text{eff}} = 0.0$  eV and changes to FM beyond  $U_{\text{eff}} \sim 1.0$  eV, consistent with previous studies [34]. The HSE06 calculation also predicts FM to be more stable than AFM by 14.2 meV per interface [Fig. 2(a), horizontal dashed lines]. In contrast with  $H_0$ , other stacking types have FM as the ground state for almost all  $U_{\text{eff}}$ , with larger enhancement toward FM for  $H_1$  than  $H_2$  for each  $U_{\text{eff}}$ . Thus, FM interlayer exchange coupling is more favored when FGT has stacking faults. Figure 2(b) confirms that  $\Delta E$  dependence on stacking type remains the same for bilayer FGT but with significantly increased magnitude compared with bulk by LDA +  $U$  or HSE06, indicating that FM interlayer exchange couplings were more favored.

Stronger FM interlayer exchange coupling for bilayer than bulk [Figs 2(a) and 2(b)] can be understood qualitatively from phenomenological theory: the Bethe-Slater curve for energy exchange with respect to interatomic distance for transition metals. Figure 2(c) compares  $\Delta E$  with respect to  $h$  calculated using  $U_{\text{eff}} = 3.0$  eV for bulk and bilayer FGT for stacking type  $H_0$ . Both curves exhibit typical shape with peaks at certain distances and decaying to zero with increasing distance, but  $\Delta E$  is significantly greater for bilayer than bulk for distances larger than the peak position.

Previous studies have shown that net interlayer exchange coupling for metallic vdW magnets is decided by two competing energies [41]. AFM configuration is preferred over FM due to the Pauli principle once interlayer hybridization of

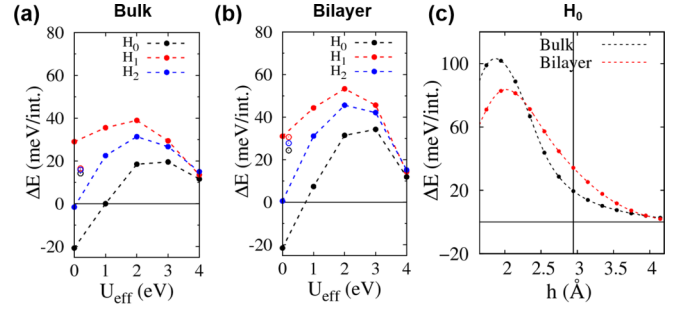


FIG. 2. Stacking-dependent interlayer magnetic coupling for bulk and bilayer Fe<sub>3</sub>GeTe<sub>2</sub> (FGT). Total energy difference between antiferromagnetic (AFM) and ferromagnetic (FM) interlayer exchange coupling configurations for (a) bulk and (b) bilayer FGT for three stacking types by LDA +  $U$ , varying Fe  $d$  Hubbard  $U_{\text{eff}} = 0-4$  eV. AFM and FM total energies,  $E_{\text{AFM}}$  and  $E_{\text{FM}}$ , respectively, per unit cell, are used to obtain  $\Delta E = (E_{\text{AFM}} - E_{\text{FM}})/2$  for bulk and  $\Delta E = E_{\text{AFM}} - E_{\text{FM}}$  for bilayer to compare interlayer exchange coupling in millielectronvolts per van der Waals (vdW) interface (meV/int.) from (a) and (b). The open circles in (a) and (b) indicate the results by HSE06 with a small horizontal offset for clarity, where  $\Delta E = 14.2$ , 16.4, and 16.0 meV/int. for  $H_0$ ,  $H_1$ , and  $H_2$ , respectively, in bulk and 24.4, 30.6, and 27.8 meV/int. in bilayer. (c)  $\Delta E$  for bulk and bilayer FGT for  $H_0$  type by LDA +  $U_{\text{eff}} = 3$  eV with varying  $h$ . Experimental distance ( $h^{\text{exp}} = 2.95 \text{ \AA}$ ) is indicated by the vertical line. Dashed lines are included for guidance to calculated data trends.

ligand  $p$  orbitals forms, and the preference is enhanced for larger energy level splitting between bonding and antibonding hybridization type orbitals with occupancies two (up and down spin) and zero, respectively. In contrast, FM configuration is favored since there is kinetic energy gain by electron hopping across the vdW gap. Figure 2(c) shows enhanced FM interlayer exchange coupling for the bilayer, assuming almost equal interlayer hopping strengths between bulk and bilayer cases, attributed to reduced Pauli potential (see later discussion).

We calculated exchange constants for bulk and bilayer FGT using Green's functions (see Sec. II) to investigate microscopic details for interlayer exchange coupling. Nearest neighbor intralayer pairs strongly favor parallel alignment with energy gain  $\sim 100$  and  $50$  meV for Fe<sup>I</sup>-Fe<sup>I</sup> or Fe<sup>I</sup>-Fe<sup>II</sup>, respectively, consistent with previous studies [42,43], with little stacking-type dependence: nearest neighbor Fe<sup>I</sup>-Fe<sup>I</sup> pairs exhibit maximal variation  $\sim 10$  meV between  $H_1$  and  $H_2$  types (see Table S5 in the Supplemental Material [25]).

We denote interlayer exchange coupling by  $J_m$ , where  $m = 1, 2, \text{ and } 3$  (or 4) refer to Fe<sup>I</sup>-Fe<sup>I</sup>, Fe<sup>II</sup>-Fe<sup>II</sup>, and Fe<sup>I</sup>-Fe<sup>II</sup> (or Fe<sup>II</sup>-Fe<sup>I</sup>) interlayer pair types, respectively (Fig. 3, solid arrows), where  $H_2$  lacking inversion symmetry causes  $J_4 \neq J_3$ . Vertical distances can exceed the shortest distance for pairs involving Fe<sup>I</sup> dumbbell atoms, indicated by  $J'_1, J'_2, J'_3,$  and  $J'_4$  (Fig. 3, dashed or dotted arrows). Table I shows calculated interlayer exchange coupling constants for three (four) types for the smallest lateral shift cases, and Table S1 in the Supplemental Material [25] shows up to third neighbor pairs with further lateral shifts contributing significantly less, which would not change the main conclusion.



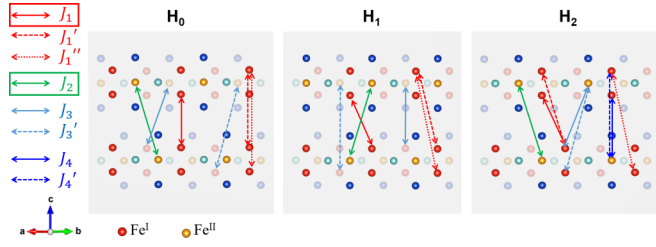


FIG. 3. Exchange constants for interlayer Fe atom pairs. Fe atoms associated with interlayer exchange coupling  $J_m$  ( $m = 1, 2, 3, 4$ ) across the van der Waals (vdW) gap, indicated by two-sided arrows with four different colors, where each Fe pair involves either  $\text{Fe}^{\text{I}}$  or  $\text{Fe}^{\text{II}}$  atoms in the lower or upper layer, respectively. Side views are the [110] direction with only two nearest atomic layers shown by unshaded (front) and shaded (rear) scheme. Red, green, and light blue indicate  $J_1$  for  $\text{Fe}^{\text{I}}\text{-Fe}^{\text{I}}$ ,  $J_2$  for  $\text{Fe}^{\text{II}}\text{-Fe}^{\text{II}}$ , and  $J_3$  for  $\text{Fe}^{\text{I}}\text{-Fe}^{\text{II}}$  or  $\text{Fe}^{\text{II}}\text{-Fe}^{\text{I}}$ , respectively, with blue color indicating  $J_4$  for  $\text{Fe}^{\text{II}}\text{-Fe}^{\text{I}}$  since  $H_2$  lacks inversion symmetry. Dashed arrows for  $m = 1, 3$ , and 4 correspond to pairs associated with  $\text{Fe}^{\text{I}}$  at further vertical distance, denoted by  $J'_1, J'_3$ , and  $J'_4$ . Left-most rectangular boxes indicate interlayer exchange constants significantly affected by stacking type ( $J_1$ ) or termination ( $J_2$ ; see Table I and above for details).

Thus,  $|J_1| \gg |J'_1|$  or  $|J'_1|$ , with significant variation between bulk and bilayer. However, magnitude increases greatly when changing from  $H_0$  to other cases (Tables I and S1 in the Supplemental Material [25], bold numbers), almost fourfold for  $H_1$ , and the number of associated pairs for both  $H_1$  and  $H_2$  is threefold that for  $H_0$ . Although  $J_2$  and  $J_3$  also exhibit non-negligible stacking dependence, the variation is significantly smaller than for  $J_1$ , and the number of interlayer pairs does not change. Thus, the enhanced FM interlayer exchange coupling for  $H_1$  and  $H_2$  in Figs. 2(a) and 2(b) is ascribed to  $J_1$ .

Considering  $m = 2$ , each bilayer stacking type has more than twice  $|J_2|$  compared with bulk (Tables I and S2 in the Supplemental Material [25], underlined numbers). Thus, we mainly attribute bulk and bilayer dependence to  $J_2$ , which is reasonable because the  $\text{Fe}^{\text{II}}$  layer in bulk is equally affected by upper and lower interfaces.

First, we investigated why  $|J_2|$  is significantly increased for bilayers compared with bulk by analyzing the electronic structures. Orbital resolved analysis (Table II) tracing over

TABLE I. Calculated interlayer exchange coupling constants for bulk and bilayer FGT. Calculated values for interlayer exchange constants  $J_m$  for  $\text{Fe}^{\text{I}}\text{-Fe}^{\text{I}}$  ( $m = 1$ ),  $\text{Fe}^{\text{II}}\text{-Fe}^{\text{II}}$  ( $m = 2$ ), and  $\text{Fe}^{\text{I}}\text{-Fe}^{\text{II}}$  ( $m = 3$ ) pair types (see Fig. 3). For  $m = 1$  and 3, associated with the  $\text{Fe}^{\text{I}}$  dumbbell, pairs ( $J'_1$  and  $J'_3$ ,  $J'_3$ ) have furthest vertical distances, and  $H_2$  contains an additional type  $\text{Fe}^{\text{II}}\text{-Fe}^{\text{I}}$  ( $m = 4$ ) due to lacking inversion symmetry. Values in the square brackets next to exchange constants denote the number of associated pairs for each  $1 \times 1$  unit cell and one vdW gap. Calculations were performed using Green's functions (see Supplemental Material [25]) with LDA and  $U_{\text{eff}} = 3$  eV. The unit is millielectronvolts. Bold  $J_1$  values or underlined  $J_2$  values indicate significant dependence of stacking type ( $H_0, H_1, H_2$ ) or termination (bulk with respect to bilayer), respectively (see text for details).

Stacking	System	$J_1, J'_1, J'_3$	$J_2$	$J_3, J'_3$	$J_4, J'_4$
$H_0$	Bulk	<b>0.95</b> [1], 0.16[2], -0.13[1]	<u>1.33</u> [3]	0.64[3], 0.50[3]	
	Bilayer	<b>1.31</b> [1], 0.53[2], 0.22[1]	<u>3.17</u> [3]	0.60[3], 0.42[3]	
$H_1$	Bulk	<b>4.00</b> [3], 0.11[6], 0.01[3]	<u>0.54</u> [3]	-0.60[1], 0.40[1]	
	Bilayer	<b>4.29</b> [3], 0.30[6], 0.10[3]	<u>1.66</u> [3]	-0.82[1], 0.14[1]	
$H_2$	Bulk	<b>1.72</b> [3], 0.12[6], -0.08[3]	<u>1.09</u> [3]	-0.48[1], 0.77[1]	0.54[3], 0.43[3]
	Bilayer	<b>2.14</b> [3], 0.30[3], 0.03[3]	<u>2.31</u> [3]	-0.91[1], 0.59[1]	0.50[3], 0.59[1]

TABLE II. Atomic orbital projection for itinerant-type interlayer exchange coupling constant for bulk and bilayer FGT.  $J_2$  decomposition for  $H_0$  into three crystal-field components of  $d$  orbital, i.e.,  $l$  or  $l' = 0$  ( $z^2$ ), 1 ( $xz, yz$ ), 2 ( $x^2 - y^2, xy$ ). The unit is millielectronvolts.

$J_2$ for $H_0$ ( $l, l'$ )	Bulk			Bilayer		
	0	1	2	0	1	2
0	1.33	0.06	0.02	3.15	0.07	0.05
1	0.06	-0.19	0.01	0.07	-0.29	0.01
2	0.02	0.01	0.00	0.07	0.01	0.00

only  $\text{Fe}^{\text{II}} d_z^2$  orbitals at  $i$ - and  $j$ -site Fe atoms comprises almost 90% of  $J_2$ . Therefore, we inspected  $\text{Fe}^{\text{II}} d_z^2$  orbital contribution to the band structure.

Figure 4(a) shows the spin-up band structure for bulk FGT with  $H_0$  type, where contributions from  $\text{Fe}^{\text{II}} d_z^2$  and Te  $p_z$  orbitals are indicated by red and blue circles, respectively. The  $\text{Fe}^{\text{II}} d_z^2$  and Te  $p_z$  orbitals form mainly four bands near the Fermi level with significant dispersion along the out-of-plane direction ( $\Gamma$  to  $A$ ). We analyzed the four Bloch orbital characteristics at  $\Gamma$  [Fig. 4(a), arrows]. Figure 4(b) shows that isosurfaces  $\psi_1$  and  $\psi_2$  have the same superposition pattern for atomic orbitals within individual layers but opposite interlayer parities, with a similar trend for  $\psi_3$  and  $\psi_4$ . Hence, bonding and antibonding characteristics between interfacial Te  $p_z$  orbitals arise as verified by crystal orbital Hamilton population (COHP) analysis [Fig. 4(a)] [44,45]. COHP is positive for  $\sim -0.8$  and 1.2 eV [Fig. 4(a), black arrows], suggesting that associated Bloch orbitals are mainly characterized by bonding type  $\psi_1$  and  $\psi_3$ , respectively, and negative at  $\sim 0.2$  and 2 eV, suggesting antibonding characteristics for  $\psi_2$  and  $\psi_4$ , respectively. Energy separation between positive bilayer peaks [Fig. 4(a), red arrows] is significantly smaller than that for bulk, indicating reduced Pauli potential for bilayers, increasing the tendency toward FM-type interlayer exchange coupling, hence the main reason for enhanced  $|J_2|$  for bilayer FGT.

As  $J_2$  involves the metallic band across the vdW gap, we considered the FGT quartet layer to study vertical distance and thickness effects. Figure 4(c) inset shows three  $J_2$  pairs with vertical interatomic distance  $z_{ij} = c/2$ , where  $c = 16.33$  Å is

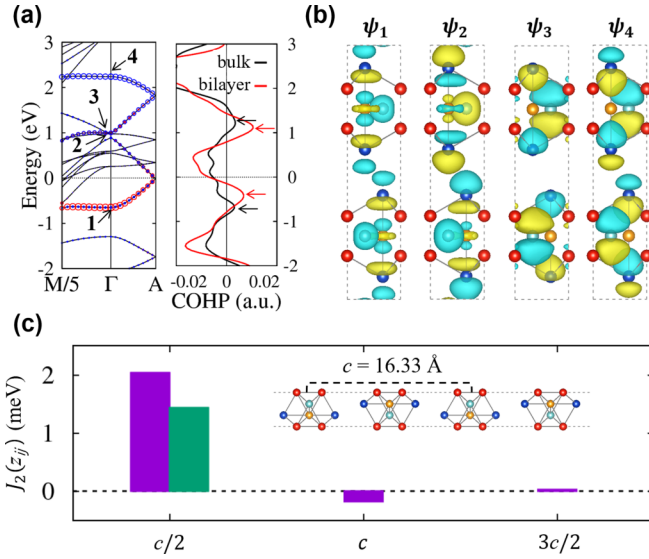


FIG. 4. Out-of-plane metallic band for bulk  $\text{Fe}_3\text{GeTe}_2$  (FGT) and itinerant-type interlayer exchange coupling for FGT quartet layer. (a) Spin-up band structure (LDA +  $U_{\text{eff}} = 3$  eV) for bulk FGT with  $H_0$  type, with  $\text{Fe}^{\text{II}} d_z^2$  and  $\text{Te } p_z$  orbital contributions indicated by red and blue circles sizes, respectively. Right panel shows crystal orbital Hamiltonian population (COHP) curves for  $\text{Te } p_z$  orbitals with respect to energy for bulk and bilayer, where positive and negative values indicate bonding and antibonding interlayer orbital hybridizations, respectively. (b) Isosurfaces (isolevel  $3 \times 10^{-5}$ ) for four Bloch orbitals at  $\Gamma$ , indicated by numbered arrows in (a) band structure, with yellow and blue colors indicating positive and negative, respectively. (c) Calculated  $J_2$  for quartet layer FGT with  $H_0$  type with respect to vertical interatomic distance for  $\text{Fe}^{\text{II}}\text{-Fe}^{\text{II}}$  varying as  $z_{ij} = c/2$ ,  $c$ , and  $3c/2$ , where  $c = 16.33$  Å is the bulk lattice parameter.  $z_{ij} = c/2$  exhibits two equivalent outer pairs and one inner pair with  $J_2(c/2) = 2.0$  and  $1.5$  meV, respectively. Similarly, there are two equivalent pairs for  $z_{ij} = c$  and one pair for  $z_{ij} = 3c/2$ .

the bulk lattice parameter, two at the outer region and one at the center. Calculated results [Fig. 4(c)] show  $J_2(c/2) = 2.0$  meV for two outer pairs is significantly smaller than that for the bilayer ( $3.17$  meV), and  $J_2(c/2) = 1.5$  meV for the inner pair is close to that for bulk ( $1.33$  meV). Thus, the effect of stacking termination is considerable only for the outermost surface layer. Similarly,  $J_2$  exhibits almost diminished magnitudes for vertical distances  $> c/2$  with negative or positive sign for  $z_{ij} = c$  or  $3c/2$ , respectively, indicating almost perfect itinerant interlayer exchange coupling shielding by the quintuple layer.

We then investigated stacking-type dependence for  $J_1$ . In contrast with  $J_2$ ,  $J_1$  has much less system (bulk vs bilayer) dependence, indicating nonitinerant-type exchange interactions favoring FM interlayer exchange coupling. Direct FM coupling between minority-spin  $p$  electrons from interfacial I atoms was shown to cause FM interlayer exchange coupling in  $\text{CrI}_3$  [14], which is similarly observable in our case.

As Tables S2–S4 in the Supplemental Material [25] show,  $\text{Fe}^{\text{I}} d_{xz}/d_{yz}$  orbitals mainly contribute to  $J_1$ , in hybridization with  $\text{Te } p_x/p_y$  orbitals. Figure 5(a) shows spin-up band structures for three stacking types, where  $\text{Fe}^{\text{I}} d_{xz}/d_{yz}$  and  $\text{Te } p_x/p_y$  orbitals contribute mainly below and above the Fermi level

(indicated by red and blue circles), respectively. Stacking type mainly affects dispersion around  $K$  and  $H$  in the Brillouin zone. Consider  $H_0$  and  $H_1$  along the  $\Gamma$ - $K$  direction whose little group contains the twofold rotation axis ( $C_{2y}$ ). The Bloch orbitals have even (odd)  $C_{2y}$  parity indicated by  $\Lambda_1$  ( $\Lambda_2$ ),  $\Lambda_3$  ( $\Lambda_4$ ) irreducible representations, respectively. For  $H_0$ , two orbitals with opposite  $C_{2y}$  parities have the same energy eigenvalue with twofold degeneracy at the  $K$ - $H$  line, whereas for  $H_1$ , their energy levels are split, except at  $H$  ( $k_z = \pi/c$ ). Such distinctive behavior originates from vanishing and nonvanishing interlayer orbital hopping at  $K$  for  $H_0$  and  $H_1$ , respectively. Figure 5, insets show isocharges for  $\Lambda_1$  and  $\Lambda_4$  Bloch orbitals at  $K$ .

We investigated symmetrical origins for dramatically different interlayer orbital hopping strengths between  $H_0$  and  $H_1$ . For monolayer FGT (Fig. S3 in the Supplemental Material [25]), associated Bloch orbitals at  $K$  have significant contribution  $\text{Te } x + iy$  with even and odd  $M_z$  parities for  $\psi_K^{\text{VBM}}$  (valence band maximum) and  $\psi_K^{\text{VBM}-1}$ , respectively, where  $M_z$  denotes mirror reflection about the central atomic layer ( $\text{Fe}^{\text{II}}\text{Ge}$ ). For bulk FGT with  $H_0$  and  $H_1$  types, once one  $\text{Te}$  layer at the vdW contact has atomic orbital symmetry  $x + iy$ , the other  $\text{Te}$  layer should have symmetry  $-x + iy$  or  $x - iy$ , to maintain even or odd  $C_{2y}$  parity, respectively. Even parity results in representations  $\Lambda_1$  from  $\psi_{\Gamma-K}^{\text{VBM}}$  and  $\Lambda_2$  from  $\psi_{\Gamma-K}^{\text{VBM}-1}$  along  $\Gamma$  to  $K$ , whereas odd parity gives  $\Lambda_4$  and  $\Lambda_3$ .

Figure 5(b) shows that interlayer hopping can be described between  $\varphi_L = x + iy$  from lower  $\text{Te}^L$  and  $\varphi_U = x - iy$  (or  $-x + iy$ ) from upper  $\text{Te}^U$  with the three nearest neighbor lateral vectors  $\tau_j$ ,  $j = 1, 2$ , and  $3$  from  $\text{Te}^L$  to  $\text{Te}^U$ . Thus, the hopping integral at  $K$  is vanishing for  $H_0$ , but  $3(V_\sigma - V_\pi)e^{-i2\pi/3}$  for  $H_1$  due to reverted  $\tau_j$ , where  $V_\sigma$  and  $V_\pi$  are hopping parameters for  $p_x$ ,  $p_y$  orbitals for  $\sigma$  and  $\pi$  bonds, respectively. This enhanced interlayer orbital hopping increases exchange integrals, hence enhancing  $J_1$ .

We investigated  $\text{CrI}_3$  bilayer with  $R\bar{3}$  and  $C2/m$  symmetries, where electron doping can strengthen FM interlayer exchange coupling for both stacking types [14]. Like  $H_0$  vs  $H_1$  for bulk FGT, the conduction band exhibits stacking-dependent band splitting near  $K$  [Fig. 5(c), dashed circle], indicating larger interlayer orbital hopping for lower symmetry  $C2/m$ . The strengthening rate for FM interlayer exchange coupling with electron doping is faster than that for  $R\bar{3}$ .

Interlayer exchange coupling effects on Curie temperature ( $T_C$ ) with stacking-type dependence are practically interesting. We used mean field theory [46],  $T_C \sim J_{\text{max}}/\ln(3\pi J_{\text{max}}/4K)$ , where  $K$  is uniaxial magnetic anisotropy, and  $J_{\text{max}}$  is the maximum eigenvalue for the exchange constant matrix [47–49]. We adopted  $K = 1.0$  meV/Fe as reported previously [30] with  $15$  Å cutoff distance for Fe spin pairs in constructing the exchange constant matrices. Estimated Curie temperatures are  $332$ ,  $350$ , and  $339$  K for  $H_0$ ,  $H_1$ , and  $H_2$  types, respectively, for bulk FGT. The  $18$  K increase changing from  $H_0$  to  $H_1$  was ascribed to interlayer  $J_1$  (Table I) and intralayer (Table S5 in the Supplemental Material [25]) exchange constant enhancements.

Finally, FM interlayer exchange coupling is significantly suppressed with reducing  $U_{\text{eff}}$  value [Fig. 2(a)], which could be related to the metallic band width associated with  $J_2$  (Fig. S4 in the Supplemental Material [25]). Therefore, we

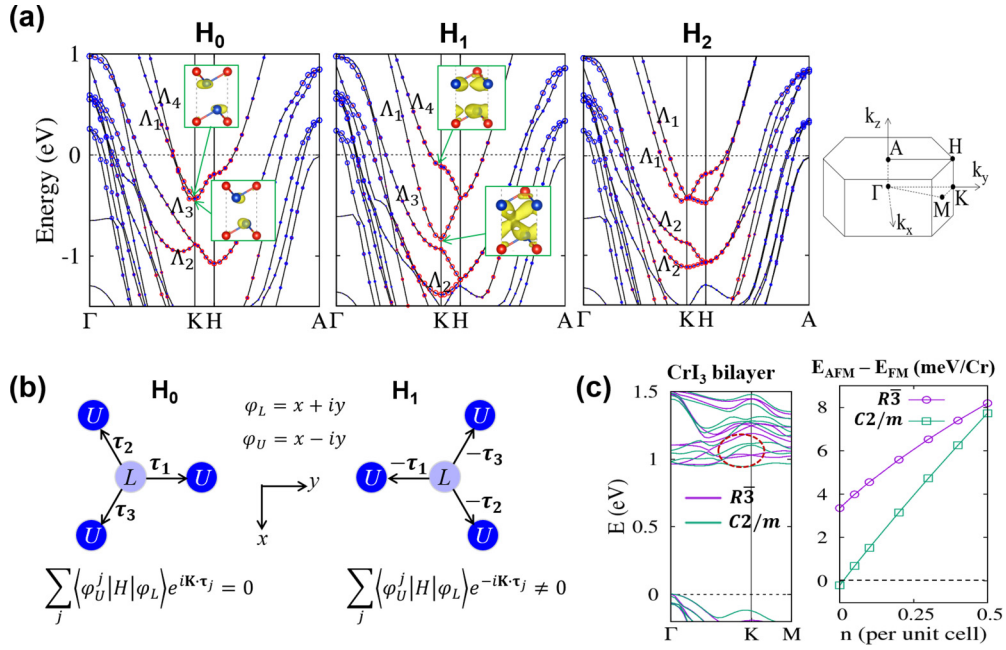


FIG. 5. Stacking-dependent interlayer orbital hopping. (a) Spin-up band structures (LDA +  $U_{\text{eff}} = 3 \text{ eV}$ ) for bulk  $\text{Fe}_3\text{GeTe}_2$  (FGT) for three stacking types with contributions from  $\text{Fe}^{\text{I}}$   $d_{xz}/d_{yz}$  and  $\text{Te}$   $p_x/p_y$  orbitals indicated by red and blue circles, respectively.  $\Lambda_{1,2}$  and  $\Lambda_{3,4}$  have even or odd parity along the  $\Gamma$ - $K$  direction under  $C_{2y}$  (twofold rotation about  $[110]$ ), whereas  $\Lambda_1$  and  $\Lambda_2$  for  $H_2$  have even or odd parity by mirror operation  $M_z$  about the central atomic layer ( $\text{Fe}^{\text{II}}\text{Ge}$ ). Insets show  $H_0$  and  $H_1$  isocharges for Bloch orbital at  $K$  with side views of adjacent four atomic layers  $\text{Fe}^{\text{I}}\text{Te}-\text{TeFe}^{\text{I}}$  at the van der Waals (vdW) gap. The Brillouin zone is given at the most right. (b) Stacking-dependent ( $H_0$  or  $H_1$ ) interlayer hopping magnitudes between two monolayer Bloch orbitals at  $K$ . Blue circles with  $L$  and  $U$  represent lateral positions for interfacial  $\text{Te}$  atoms from lower and upper layers, respectively, at the vdW contact, with relative lateral positions  $\tau_j$  ( $j = 1, 2, 3$ ). (c) Spin-up band structures for bilayer  $\text{CrI}_3$  with two stacking symmetries, where dashed circle indicates stacking-dependent band splitting similar to  $H_0$  vs  $H_1$  in bulk FGT. Right panel shows calculated interlayer exchange energy for bilayer  $\text{CrI}_3$  with increasing number of electrons ( $n$ ) per unit cell. We used the PBEsol density functional theory (DFT) functional for  $\text{CrI}_3$  with Hubbard  $U_{\text{eff}} = 3.0 \text{ eV}$  [14].

investigated how the substrate influences effective  $U$  because even weakly interacting vdW interface could reduce it via nonlocal screening. We considered two extreme electronic structure types for the same vdW substrate: semiconducting and metallic  $\text{MoTe}_2$ , and calculated effective  $U$  values using the constrained random phase approximation. Figure S5 in the Supplemental Material [25] shows that effective  $U$  is smaller for metallic substrate ( $1T\text{-MoTe}_2$ ) by  $\sim 0.2 \text{ eV}$  compared with semiconducting substrate ( $2H\text{-MoTe}_2$ ) for heterostructure monolayer FGT on top of  $\text{MoTe}_2$ , which could be mainly due to enhanced screening by zero-gap electrons. In addition, such zero-gap electrons in a certain semiconductor substrate might be activated by an electrical manner [50,51].

#### IV. CONCLUSIONS

We performed DFT calculations to investigate the interlayer exchange coupling in FGT. FM interlayer exchange coupling is enhanced by reducing stacking symmetry and the layer number, where the former is caused by enhanced interlayer orbital hopping and the latter by itinerant-type exchange coupling with reduced Pauli potential. We also showed

that itinerant-type FM interlayer exchange coupling could be weakened by nonlocal Coulomb interaction screening, which can be experimentally achieved by placing two-dimensional FGT on substrates of various dielectric constants. Thus, in this paper, we provide guidance to rationally control FGT interlayer exchange coupling by engineering stacking configuration and dielectric environment.

#### ACKNOWLEDGMENTS

This work was supported by the National Research Foundation of Korea (Basic Science Research Program: No. 2021R1A2C1006039, No. 2019R1A4A1029237, and No. 2016R1D1A1B02008461). K. Kim acknowledges support from KAERI Internal R&D Program (No. 524460-21). The supercomputing resources including technical support are from the National Supercomputing Center KISTI (No. KSC-2021-CRE-0188, No. KSC-2020-CRE-0251) and the UNIST Supercomputing Center. C.G. acknowledges the grants from Northrop Grumman Mission Systems' University Research Program, Naval Air Warfare Center Aircraft Division, and Army Research Laboratory Cooperative Agreement No. W911NF-19-2-0181.

[1] C. Gong, L. Li, Z. Li, H. Ji, A. Stern, Y. Xia, T. Cao, W. Bao, C. Wang, Y. Wang *et al.*, Discovery of intrinsic ferromagnetism in

two-dimensional van der Waals Crystals, *Nature (London)* **546**, 265 (2017).



- [2] B. Huang, G. Clark, E. Navarro-Moratalla, D. R. Klein, R. Cheng, K. L. Seyler, D. Zhong, E. Schmidgall, M. A. McGuire, D. H. Cobden *et al.*, Layer-dependent ferromagnetism in a van der Waals crystal down to the monolayer limit, *Nature (London)* **546**, 270 (2017).
- [3] C. Gong and X. Zhang, Two-dimensional magnetic crystals and emergent heterostructure devices, *Science* **363**, eaav4450 (2019).
- [4] Z. Wang, I. Gutiérrez-Lezama, N. Ulbrig, M. Kroner, M. Gibertini, T. Taniguchi, K. Watanabe, A. Imamoğlu, E. Giannini, and A. F. Morpurgo, Very large tunneling magnetoresistance in layered magnetic semiconductor CrI<sub>3</sub>, *Nat. Commun.* **9**, 2516 (2018).
- [5] S. Albarakati, C. Tan, Z.-J. Chen, J. G. Partridge, G. Zheng, L. Farrar, E. L. H. Mayes, M. R. Field, C. Lee, Y. Wang *et al.*, Antisymmetric magnetoresistance in van der Waals Fe<sub>3</sub>GeTe<sub>2</sub>/graphite/Fe<sub>3</sub>GeTe<sub>2</sub> trilayer heterostructures, *Sci. Adv.* **5**, eaaw0409 (2019).
- [6] J. Grollier, D. Querlioz, K. Y. Camsari, K. Eveersch-Sitte, S. Fukami, and M. D. Stiles, Neuromorphic spintronics, *Nat. Electronics* **3**, 360 (2020).
- [7] X.-F. Su, Z.-L. Gu, Z.-Y. Dong, and J.-X. Li, Topological magnons in a one-dimensional itinerant flatband ferromagnet, *Phys. Rev. B* **97**, 245111 (2018).
- [8] C. Tan, J. Lee, S. G. Jung, T. Park, S. Albarakati, J. Partridge, M. R. Field, D. G. McCulloch, L. Wang, and C. Lee, Hard magnetic properties in nanoflake van der Waals Fe<sub>3</sub>GeTe<sub>2</sub>, *Nat. Commun.* **9**, 1554 (2018).
- [9] C.-K. Tian, C. Wang, W. Ji, J.-C. Wang, T.-L. Xia, L. Wang, J.-J. Liu, H.-X. Zhang, and P. Cheng, Domain wall pinning and hard magnetic phase in Co-doped bulk single crystalline Fe<sub>3</sub>GeTe<sub>2</sub>, *Phys. Rev. B* **99**, 184428 (2019).
- [10] N. Sivadas, S. Okamoto, X. Xu, C. J. Fennie, and D. Xiao, Stacking-dependent magnetism in bilayer CrI<sub>3</sub>, *Nano Lett.* **18**, 7658 (2018).
- [11] N. Ubrig, Z. Wang, J. Teyssier, T. Taniguchi, K. Watanabe, E. Giannini, A. F. Morpurgo, and M. Gibertini, Low-temperature monoclinic layer stacking in atomically thin CrI<sub>3</sub> crystal, *2D Mater.* **7**, 015007 (2020).
- [12] D. Soriano, C. Cardoso, and J. Fernández-Rossier, Interplay between interlayer exchange and stacking in CrI<sub>3</sub> bilayers, *Solid State Commun.* **299**, 113662 (2019).
- [13] S. W. Jang, M. Y. Jeong, H. Yoon, S. Ryee, and M. J. Han, Microscopic understanding of magnetic interaction in bilayer CrI<sub>3</sub>, *Phys. Rev. Materials* **3**, 031001(R) (2019).
- [14] P. Jiang, C. Wang, D. Chen, Z. Zhong, Z. Yuan, Z.-Y. Lu, and W. Ji, Stacking tunable interlayer magnetism in bilayer CrI<sub>3</sub>, *Phys. Rev. B* **99**, 144401 (2019).
- [15] C. Lei, B. L. Chittari, K. Nomura, N. Banerjee, J. Jung, and A. H. MacDonald, Magnetoelectric response of antiferromagnetic CrI<sub>3</sub> bilayers, *Nano Lett.* **21**, 1948 (2021).
- [16] L. Thiel, Z. Wang, M. A. Tschudin, D. Rohner, I. Gutiérrez-Lezama, N. Ubrig, M. Gibertini, E. Giannini, A. F. Morpurgo, and P. Maletinsky, Probing magnetism in 2D materials at the nanoscale with single-spin microscopy, *Science* **364**, 973 (2019).
- [17] T. Song, Z. Fei, M. Yankowitz, Z. Lin, Q. Jiang, K. Hwangbo, Q. Zhang, B. Sun, T. Taniguchi, K. Watanabe, M. A. McGuire *et al.*, Switching 2D magnetic states via pressure tuning of layer stacking, *Nat. Mater.* **18**, 1298 (2019).
- [18] T. Li, S. Jiang, N. Sivadas, Z. Wang, Y. Xu, D. Weber, J. E. Goldberger, K. Watanabe, T. Taniguchi, C. J. Fennie *et al.*, Pressure-controlled interlayer magnetism in atomically thin CrI<sub>3</sub>, *Nat. Mater.* **18**, 1303 (2019).
- [19] W. Chen, Z. Sun, Z. Wang, L. Gu, X. Xu, S. Wu, and C. Gao, Direct observation of van der Waals stacking-dependent interlayer magnetism, *Science* **366**, 983 (2019).
- [20] D. R. Klein, D. MacNeill, Q. Song, D. T. Larson, S. Fang, M. Xu, R. A. Ribeiro, P. C. Canfield, E. Kaxiras, R. Comin, and P. Jarillo-Herrero, Enhancement of interlayer exchange in an ultrathin two-dimensional magnet, *Nat. Phys.* **15**, 1255 (2019).
- [21] K. Kim, J. Seo, E. Lee, K.-T. Ko, B. S. Kim, B. G. Jang, J. M. Ok, J. Lee, Y. J. Jo, W. Kang, J. H. Shim *et al.*, Large anomalous Hall current induced by topological nodal lines in a ferromagnetic van der Waals Semimetal, *Nat. Mater.* **17**, 794 (2018).
- [22] G. Kresse and J. Furthmüller, Efficient iterative schemes for *ab initio* total-energy calculations using a plane-wave basis set, *Phys. Rev. B* **54**, 11169 (1996).
- [23] G. Kresse and J. Hafner, *Ab initio* molecular dynamics for liquid metals, *Phys. Rev. B* **47**, 558 (1993).
- [24] A. I. Liechtenstein, M. I. Katsnelson, V. P. Antropov, and V. A. Gubanov, Local spin density functional approach to the theory of exchange interactions in ferromagnetic metals and alloys, *J. Magn. Magn. Mat.* **67**, 65 (1987).
- [25] See Supplemental Material at <http://link.aps.org/supplemental/10.1103/PhysRevB.105.014406> for the effect of J on the interlayer exchange energy (Fig. S1), interlayer binding energy curves for various DFT functionals (Fig. S2), the symmetry type of Bloch orbitals at K for monolayer FGT (Fig. S3), fat band structure along  $\Gamma$  to A with varying U and interlayer distance (Fig. S4), substrate-dependent onsite Coulomb parameter (Fig. S5), a full list of interlayer exchange constants for extended neighbors (Table S1), orbital decomposed interlayer exchange constants for three stacking types (Tables S2–S4), and intralayer exchange constants for three stacking types (Table S5).
- [26] D. M. Korotin, V. V. Mazurenko, V. I. Anisimov, and S. V. Streltsov, Calculation of exchange constants of the Heisenberg model in plane-wave-based methods using the Green's function approach, *Phys. Rev. B* **91**, 224405 (2015).
- [27] A. A. Mostofi, J. R. Yates, G. Pizzi, Y.-S. Lee, I. Souza, D. Vanderbilt, and N. Marzari, An updated version of WANNIER90: a tool for obtaining maximally-localised Wannier functions, *Comput. Phys. Commun.* **185**, 2309 (2014).
- [28] A. F. May, S. Calder, C. Cantoni, H. Cao, and M. A. McGuire, Magnetic structure and phase stability of the van der Waals bonded ferromagnet Fe<sub>3-x</sub>GeTe<sub>2</sub>, *Phys. Rev. B* **93**, 014411 (2016).
- [29] J. Yi, H. Zhuang, Q. Zou, Z. Wu, G. Cao, S. Tang, S. A. Calder, P. R. C. Kent, D. Mandrus, and Z. Gai, Competing antiferromagnetism in a quasi-2D itinerant ferromagnet: Fe<sub>3</sub>GeTe<sub>2</sub>, *2D Mater.* **4**, 011005 (2017).
- [30] H. L. Zhuang, P. R. C. Kent, and R. G. Hennig, Strong anisotropy and magnetostriction in the two-dimensional Stoner ferromagnet Fe<sub>3</sub>GeTe<sub>2</sub>, *Phys. Rev. B* **93**, 134407 (2016).
- [31] J.-X. Zhu, M. Janoschek, D. S. Chaves, J. C. Cezar, T. Durakiewicz, F. Ronning, Y. Sassa, M. Mansson, B. L. Scott, N. Wakeham, E. D. Bauer, and J. D. Thompson, Electronic

- correlation and magnetism in the ferromagnetic metal  $\text{Fe}_3\text{GeTe}_2$ , *Phys. Rev. B* **93**, 144404 (2016).
- [32] Y. Zhang, H. Lu, X. Zhu, S. Tan, W. Feng, Q. Liu, W. Zhang, Q. Chen, Y. Liu, X. Luo, D. Xie *et al.*, Emergence of Kondo lattice behavior in a van der Waals itinerant ferromagnet,  $\text{Fe}_3\text{GeTe}_2$ , *Sci. Adv.* **4**, eaao6791 (2018).
- [33] J. Xiao and B. Y., An electron-counting rule to determine the interlayer magnetic coupling of the van der Waals materials, *2D Mater.* **7**, 045010 (2020).
- [34] X. Kong, G. D. Nguyen, J. Lee, C. Lee, S. Calder, A. F. May, Z. Gai, A.-P. Li, L. Liang, and T. Berlijn, Interlayer magnetism in  $\text{Fe}_{3-x}\text{GeTe}_2$ , *Phys. Rev. Materials* **4**, 094403 (2020).
- [35] S. W. Jang, H. Yoon, M. Y. Jeong, S. Ryee, H.-S. Kim, and M. J. Han, Origin of ferromagnetism and the effect of doping on  $\text{Fe}_3\text{GeTe}_2$ , *Nanoscale* **12**, 13501 (2020).
- [36] S. Zhou, J. Han, S. Dai, J. Sun, and D. J. Srolovitz, Van der Waals bilayer energetics: generalized stacking-fault energy of graphene, boron nitride, and graphene/boron nitride bilayers, *Phys. Rev. B* **92**, 155438 (2015).
- [37] H. B. Cao, A. Banerjee, J.-Q. Yan, C. A. Bridges, M. D. Lumsden, D. G. Mandrus, D. A. Tennant, B. C. Chakoumakos, and S. E. Nagler, Low-temperature crystal and magnetic structure of  $\alpha\text{-RuCl}_3$ , *Phys. Rev. B* **93**, 134423 (2016).
- [38] J. Seo, D. Y. Kim, E. S. An, K. Kim, G.-Y. Kim, S.-Y. Hwang, D. W. Kim, B. G. Jang, H. J. Kim, G. Eom, S. Y. Seo *et al.*, Nearly room temperature ferromagnetism in a magnetic metal-rich van der Waals metal, *Sci. Adv.* **6**, eaay8912 (2020).
- [39] J. Stahl, E. Shlaen, and D. Johrendt, The van der Waals ferromagnets  $\text{Fe}_{5-\delta}\text{GeTe}_2$  and  $\text{Fe}_{5-\delta-x}\text{Ni}_x\text{GeTe}_2$ —crystal structure, stacking faults, and magnetic properties, *Z. Anorg. Allg. Chem.* **644**, 1923 (2018).
- [40] A. F. May, D. Ovchinnikov, Q. Zheng, R. Hermann, S. Calder, B. Huang, Z. Fei, Y. Liu, X. Xu, and M. A. McGuire, Ferromagnetism near room temperature in the cleavable van der Waals crystal  $\text{Fe}_5\text{GeTe}_2$ , *ACS Nano* **13**, 4436 (2019).
- [41] C. Wang, X. Zhou, L. Zhou, Y. Pan, Z.-Y. Lu, X. Wan, X. Wang, and W. Ji, Bethe-Slater-curve-like behavior and interlayer spin-exchange coupling mechanisms in two-dimensional magnetic bilayers, *Phys. Rev. B* **102**, 020402(R) (2020).
- [42] Z.-X. Shen, X. Bo, K. Cao, Xi. Wan, and L. He, Magnetic ground state and electron-doping tuning of Curie temperature in  $\text{Fe}_3\text{GeTe}_2$ : first-principles studies, *Phys. Rev. B* **103**, 085102 (2021).
- [43] Y. Deng, Y. Yu, Y. Song, J. Zhang, N. Z. Wang, Z. Sun, Y. Yi, Y. Z. Wu, S. Wu, J. Zhu, J. Wang *et al.*, Gate-tunable room-temperature ferromagnetism in two-dimensional  $\text{Fe}_3\text{GeTe}_2$ , *Nature (London)* **563**, 94 (2018).
- [44] R. Dronskowski and P. E. Blochl, Crystal orbital Hamilton populations (COHP): energy-resolved visualization of chemical bonding in solids based on density-functional calculations, *J. Phys. Chem.* **97**, 8617 (1993).
- [45] V. L. Deringer, A. L. Tchougréeff, and R. Deringer, Crystal orbital Hamilton population (COHP) analysis as projected from plane-wave basis sets, *J. Phys. Chem. A* **115**, 5461 (2011).
- [46] M. Bander and D. L. Mills, Ferromagnetism of ultrathin films, *Phys. Rev. B* **38**, 12015 (1988).
- [47] E. Şaşıoğlu, L. M. Sandratskii, and P. Bruno, First-principles calculation of the intersublattice exchange interactions and curie temperatures of the full Heusler alloys  $\text{Ni}_2\text{MnX}$  ( $X = \text{Ga}, \text{In}, \text{Sn}, \text{Sb}$ ), *Phys. Rev. B* **70**, 024427 (2004).
- [48] J. Liu, Y. You, I. Batashev, Y. Gong, X. You, B. Huang, F. Zhang, X. Miao, F. Xu, N. V. Dijk, and E. Brück, Design of Reversible Low-Field Magnetocaloric Effect at Room Temperature in Hexagonal  $\text{MnMX}$  ferromagnets, *Phys. Rev. Appl.* **13**, 054003 (2020).
- [49] S. Singh, L. Caron, S. W. D'Souza, T. Fichtner, G. Porcari, S. Fabbrici, C. Shekhar, S. Chadov, M. Solzi, and C. Felser, Large magnetization and reversible magnetocaloric effect at the second-order magnetic transition in Heusler materials, *Adv. Mater.* **28**, 3321 (2016).
- [50] S.-J. Gong, C. Gong, Y.-Y. Sun, W.-Y. Tong, C.-G. Duan, J.-H. Chu, and X. Zhang, Electrically induced 2D half-metallic antiferromagnets and spin field effect transistors, *Proc. Natl. Acad. Sci. USA* **115**, 8511 (2018).
- [51] C. Gong, E. M. Kim, Y. Wang, G. Lee, and X. Zhang, Multiferroicity in atomic van der Waals heterostructures, *Nat. Commun.* **10**, 2657 (2019).